Journal of Chromatography A 1737 (2024) 465460

Contents lists available at ScienceDirect

Journal of Chromatography A

journal homepage: www.elsevier.com/locate/chroma

Determination of particle number concentration for biological particles using AF4-MALS: Dependencies on light scattering model and refractive index

Christine L. Plavchak [a], Allison Z. Werner [b], Elizabeth Betz [a], Davinia Salvachúa [b], Gregg T. Beckham [b], S. Kim Ratanathanawongs Williams [a,*]

[a] Department of Chemistry, Colorado School of Mines, 1500 Illinois St., Golden, CO 80401, United States
[b] Renewable Resources and Enabling Sciences Center, National Renewable Energy Laboratory, Golden, CO 80401, United States

ARTICLE INFO

Keywords:
Multiangle light scattering
Particle counting
Errors in particle number concentration
Refractive index
Asymmetrical flow field-flow fractionation
Outer membrane vesicles

ABSTRACT

Determining accurate counts and size distributions for biological particles (bioparticles) is crucial in wide-ranging fields, but current methods to this end are susceptible to bias from polydispersity in size. This bias can be mitigated by incorporating a separation step prior to characterization. For this reason, asymmetrical flow field-flow fractionation (AF4) with on-line multiangle light scattering (MALS) has become an important platform for determining particle size. AF4-MALS has also been increasingly used to report particle concentration, particularly for complex biological particles, yet the impact of light scattering models and particle refractive indices (RI) have not been quantitatively evaluated. Here, we develop an analysis workflow using AF4-MALS to simultaneously separate and determine particles sizes and concentrations. The impacts of the MALS particle counting model used to process data and the chosen RI value(s) on particle counts are systematically assessed for polystyrene latex (PSL) particles and bacterial outer membrane vesicles (OMVs) in the 20–500 nm size range. Across spherical models, PSL and OMV particle counts varied up to 13 % or 200 %, respectively. For the coated-sphere model used in the analysis of OMV samples, the sphere RI value greatly impacts particle counts. As the sphere RI value approaches the RI of the suspending medium, the model becomes increasingly sensitive to the light scattering signal-to-noise ratio ultimately causing erroneous particle counts. Overall, this work establishes the importance of selecting appropriate MALS models and RI values for bioparticles to obtain accurate counts and provides an AF4-MALS method to separate, enumerate, and size polydisperse bioparticles.

1. Introduction

The measurement of physicochemical properties of polydisperse, complex biological particles (bioparticles) is an essential step towards understanding their function and harnessing their properties. Characteristics such as size and particle concentration are key attributes yet there lacks a standardized way to measure and report these values across different research areas. While much attention has focused on developing reproducible and accurate sizing techniques for < 500 nm diameter particles, lesser attention has been given to particle counting until recently. This interest has been driven by the realization that bioparticles can play important roles in processes such as cell-cell signaling via exosomes [1], function as biomarkers [2,3], and be used as therapeutic tools [4]. In these scenarios, particle size distribution and concentration are important primary characteristics that are relatable to observed function, stability, potency, and batch-to-batch or biological reproducibility.

Multiple techniques rooted in different principles have been used to determine particle size and/or concentrations of extracellular vesicles, lipid nanoparticle drug carriers, etc. [5] Current methods include tunable resistive-pulse sensing (TRPS) [6,7], conventional Coulter counter (CC) [8], dynamic light scattering (DLS) [9], flow cytometry (FC) [5], nanoparticle tracking analysis (NTA) [10], and multiangle light scattering (MALS) [11] However, ensemble methods such as DLS and MALS only provide averages and do not capture information regarding size distributions within the sample. Discrete methods that examine particle-by-particle such as TRPS, CC, and FC are not sensitive enough to analyze small particles (e.g., < 30 nm in diameter) and all

* Corresponding author.
E-mail address: krwillia@mines.edu (S. Kim Ratanathanawongs Williams).

https://doi.org/10.1016/j.chroma.2024.465460
Received 16 September 2024; Received in revised form 17 October 2024; Accepted 18 October 2024
Available online 19 October 2024

methods except for FC (which requires labeling) often cannot readily accommodate large particle size distributions within a sample (e.g., 20–500 nm). The latter is because of either instrumental constraints (e.g., needing multiple apertures and aperture blockage (CC), buildup of particles around tunable pores (TRPS), camera setting sensitivities (NTA) [12,13] or larger particles disproportionately impacting light scattering signal intensities (MALS)). Furthermore, incorrect use of the formalisms or shape-specific models in processing MALS data may introduce significant errors in reported values such as molar mass and size of polymers [14]. In the absence of certified particle count standards, comparisons between multiple techniques are the means to assessing methodological robustness and accuracy [5,15,16] but care must be taken to understand each technique's limitations.

Particle separation can mitigate biases by creating more monodisperse sample subpopulations prior to sizing and quantifying. Two of the techniques mentioned previously, NTA and MALS, have been coupled to size exclusion chromatography (SEC) and asymmetrical flow field-flow fractionation (AF4) and NTA has been also been utilized as an offline, post-fractionation counting technique [15,17,18]. NTA determines particle size and count by optically tracking the Brownian motion of particles in solution whereas MALS measures the light scattering intensity from particles at different known angles and fits these intensities to light scattering formalisms or shape-specific models to obtain size and count information. Because of its ready availability, AF4-MALS has been increasingly used to determine particle concentration particularly for bioparticles such as virus-like particles, lipid-based nanocarriers [5,11,19–21] and extracellular vesicles [22–24]. While the importance of accurate refractive index values has been noted, none of these studies *quantitatively* examined the impact of analyte parameters and data processing (e.g., refractive index (RI) values and light scattering model, respectively) on the reported particle concentrations.

To address this knowledge gap, an analytical AF4-MALS method suitable for dilute sample suspensions of 20 nm to ~500 nm size particles was developed. The effect of light scattering model and RI on particle counts was then systematically evaluated for polystyrene latex (PSL) standards and bacterial outer membrane vesicles (OMVs). OMVs were chosen as an exemplary bioparticle for this study as they are polydisperse (e.g., 25 to 500 nm [25–27]) and have a core-shell structure with a varying shell composition based on differing ratios of lipoproteins, phospholipids and proteins [28] all of which affect RI. The AF4-MALS method we present provides simultaneous size-based separation and particle concentration of PSL standards and OMVs. Notably, this study, for the first time, *quantitatively* assesses the impact of variations in analyte refractive index values, the model chosen to process MALS data, and the impact of the signal-to-noise ratio of the light scattering intensity on particle concentration.

2. MALS particle counting theory

Regarding the use of light scattering theories for particle counting, there are subtle differences in particle counting equations [29,30] and it is important to understand the assumptions for data analysis and interpretation. Additional details regarding both Mie theory and Rayleigh-Gans-Debye (RGD) approximations can be found in the Supplemental Information.

2.1. Mie theory

The use of Mie theory in particle counting is centered around obtaining the exact solution of the interaction of light with a spherical particle. When using this theory for determining particle concentration, the following equation is used

$$N = \frac{k^2 R(\theta)}{i\,(\theta)} \tag{1}$$

where N is the numbers of particles per milliliter, $k = 2\pi n_o/\lambda_o$ where n_o is the refractive index of the solvent and λ_o is the wavelength of the laser, $R(\theta)$ is the Rayleigh ratio ($R(\theta) \propto I_{\theta S}/I_0$), and $i(\theta)$ is the differential intensity or single particle scattering function (Eq. S2). The $i(\theta)$ equation's angular dependence on particle size suggests that the measured light scattering intensities and selection of detector angles may be important considerations in data analysis. Particle counting using Mie theory can be applied to particles spanning a range of 20–500 nm in diameter (depending on instrumental limitations such as laser wavelength) [29], but the reliability of using this model will also be influenced by RI values used in data analysis.

2.2. Rayleigh-Gans-Debye (RGD) approximation

While the RGD approximation is more widely used in the different formalisms for determining molecular weight and root mean square radius, a similar equation to Mie theory can be used for particle concentration.

Assuming an accurate extrapolation of the light scattering data to the 0° angle ($R(0)$), and a uniform density, a similar particle counting equation is derived (see Supplemental Information)

$$N \propto \frac{R(0)}{V_i^2} \tag{2}$$

where V_i^2 is the volume of the particle. While there is no exact relationship that dictates the upper limit for the RGD approximation, one may consider the analyte diameter at which isotropic scattering occurs. This has been described as a range of 1/10th to 1/20th of the wavelength of the laser [31,32]. For analytes beyond that diameter the light scattered by the analyte becomes more asymmetrical, giving rise to angular dependence. This results in a transition from Rayleigh to Mie scattering, limiting the use of the RGD approximation for a more polydisperse sample (20–500 nm) [31].

2.3. Assumptions to consider for MALS particle counting

In addition to both Mie theory and RGD approximation having different size limitations, there are other assumptions that pertain to both theories when used for particle counting. These assumptions, related to Eqs. (1) and (2) consist of the following: 1) particles are monodisperse in size, 2) there are zero contributions of scattering from the solvent, giving an absolute Rayleigh ratio (R(θ)) (where $R(\theta_i) = R_s(\theta_i) - R_f(\theta_i)$ and θ_i is the known angle, R_s is the Rayleigh ratio of the solution and R_f is the Rayleigh ratio of carrier fluid), 3) real and imaginary refractive index (RI) values are known, and 4) the RGD approximation can be used when particle refractive index is close to the RI value of the suspending fluid ($n_a/n_o - 1 \ll 1$) [30,33]. It should be known that the latter assumption is solely for the RGD approximation, and is not considered for the models under the Lorenz-Mie theory which are discussed in the next section.

2.4. MALS particle count models

Sphere models for particle counting are the focus of this work. Three different spherical models can be used to analyze particles and their underlying theories follow either Mie theory or the RGD approximation. The "Lorenz-Mie" and "coated sphere" models use Mie theory while "sphere" model uses the RGD approximation.

To successfully use these models, all three require sphere radius information which can be determined by online MALS along with the analytes' absolute and imaginary RI values. The sphere and Lorenz-Mie models require only one RI value whereas the coated sphere model needs two RI values (sphere and shell RI) and knowledge of the shell thickness.

3. Experimental section

3.1. Materials and methods

3.1.1. Polystyrene latex and buffer preparation

National Institute of Standards and Technology Traceable Size Standards (also known as Duke polystyrene latex (PSL) particles) with sizes of 22, 100, and 496 nm were obtained from Thermo Fisher Scientific (Waltham, MA) and used for the AF4 method development. These standards are 1 % solids based on their Certification of Analysis and were subsequently diluted with the AF4 carrier fluid which consisted of 0.02 % sodium azide (Sigma-Aldrich, St. Louis, MO) and 0.05 % FL-70 surfactant (Thermo Fisher Scientific, Waltham, MA) in deionized 18.2 MΩ·cm water. For OMV separation, 150 mM phosphate buffered saline (PBS) was prepared with sodium chloride (Thermo Fisher Scientific, Waltham, MA), potassium chloride (Mallinckrodt Chemical, St. Louis, MO), sodium phosphate dibasic (Thermo Fisher Scientific, Waltham, MA), and potassium phosphate monobasic (Mallinckrodt Chemical, St. Louis, MO).

3.1.2. Production and isolation of OMVs

Pseudomonas putida KT2440 (*P. putida)* was inoculated into 50 mL of M9 minimal media (6.78 g/L Na_2HPO_4, 3 g/L KH_2PO_4, 0.5 g/L NaCl, 1 g/L NH_4Cl, 2 mM $MgSO_4$, 100 μM $CaCl_2$, and 18 μM $FeSO_4$) supplemented with 5 g/L glucose ("lignin-free" condition) or 5 g/L glucose plus 25 % (v/v) alkaline liquor from corn stover pretreatment with NaOH ("lignin-rich" condition) in biological triplicate. These cultivation conditions were selected based on a previous study that suggested that OMV sizes depend on the media composition [34]. All chemicals other than 'the lignin-rich' liquor, which was made in-house as has been described previously [35] were purchased from Sigma-Aldrich (St. Louis, MO). Cultivation conditions and OMV isolation and purification were performed as previously describe [34].

3.2. Asymmetrical flow field-flow fractionation (AF4) and multi-angle light scattering (MALS)

All experiments were performed using an AF2000 system (Postnova Analytics, Salt Lake City, UT) coupled to a SPD-20A UV/Vis detector (Shimadzu, Columbia, MD), and a multi-angle light scattering (MALS) DAWN HELEOS II with a wavelength of 658 nm (Wyatt Technology Corporation, Santa Barbara, CA). The channel was formed with a tip-to-outlet length of 27.5 cm, breadth at channel inlet of 2 cm, breadth of channel outlet of 0.5 cm, and a spacer with a nominal thickness of 350 μm. The accumulation wall was a 30 kDa molecular weight cutoff regenerated cellulose membrane (Postnova Analytics, Salt Lake City, UT). A 0.1 μm inline filter (Merck Millipore Ltd, Darmstadt, Germany) between the HPLC pump and the AF4 channel was used to filter 0.02 % sodium azide and 0.05 % FL-70 surfactant along with 150 mM PBS as the two carrier fluids used in this study.

The initial AF4-UV-MALS method had a focusing time of either 10 or 15 min, the injection flow rate was 0.2 mL/min, the detector flow rate was 0.5 mL/min, and the sample injection volume was either 200, 500, and 1000 μL. The crossflow rate was programmed to start at 1.0 mL/min during focusing, then decreased linearly to 0.1 mL/min over 10 min, held at 0.1 mL/min for 20 min, and then turned off. For OMV fractionation, the isocratic hold at 0.1 mL/min was shortened to 2.5 min after testing the methods with the different OMV samples used in this study.

3.3. Particle counting analysis using MALS

Data acquisition and particle counting analysis were performed using ASTRA 7.3.2.21 (Wyatt Technology Corporation, Santa Barbara, CA). The MALS detector was normalized using bovine serum albumin (BSA) (Sigma-Aldrich). For each PSL size, triplicate runs were injected into the AF4 using a 200 μL sample loop and the AF4 method described in the previous section. The 22 and 100 nm PSL particles were diluted by 200, 400, 1000, or 2,000x and 90 % of the MALS laser power was used. The 496 nm particles were diluted by 1000, 2000, 4000, and 8,000x and the MALS laser power was set to 25 % to prevent saturation of the low-angle detectors (detectors 1–8). Using the ASTRA software, the sphere and Lorenz-Mie models were selected and RI = 1.58 for PSL. Detectors 2–18, 5–18, and 9–18 were used for data analysis of the 100 and 496 nm PSL. Corresponding detector angles can be seen in Table S1.

For OMV particle counting, the MALS laser power was set to 90 %, and 'Heavy' was chosen as the despiking level for the MALS signal. In addition to the sphere and Lorenz-Mie models, the coated sphere model was also examined. An RI range of 1.35–1.65 was used to encompass the range of composition of the OMVs. Detector selection was determined by examining the best fit (R^2 value) to the spherical model used at the peak maximum of each sample, which can be found in the "Molar Mass & Radius from LS" procedure in the ASTRA software. For lignin-free samples, detectors 8–17 were selected while detectors 7–17 were chosen for the lignin-rich samples. Additional details regarding the RI range and detector selection will be discussed in the following section.

For both PSL and OMVs, the number of particles were obtained from the summary report from the ASTRA software. The particle concentration or number of particles per milliliter was obtained using the volume of the analyte peak. The volume was determined from the area under the peak multiplied by the detector flow rate.

4. Results and discussion

4.1. AF4-MALS method for size-based separation and enumeration

4.1.1. Adaptation of AF4 method for large sample volume injections

Current AF4 separations for bioparticles or macromolecules use injection volumes that span 10–150 μL [36,37]. While these volumes are suitable for characterization, they may not be suitable for fraction collection and further offline analyses due to significant sample dilution. This may also lead to low light scattering intensities thereby impacting size and count analysis [5]. To increase the measured light scattering intensity and decrease the number of AF4 runs needed to produce sufficient quantities of subpopulations for further analysis, injection volumes of 200, 500, and 1000 μL were investigated. A PSL mixture of 22, 100, and 496 nm particles was chosen due to the size range of the bacterial OMVs (25–500 nm). Experiments contained the same sample mass, but in larger injection volumes, and retention times and sample recoveries were evaluated for the different sample loop volumes.

As injection volume increased, consistent retention times and peak areas were observed for each species in the PSL mixture showing

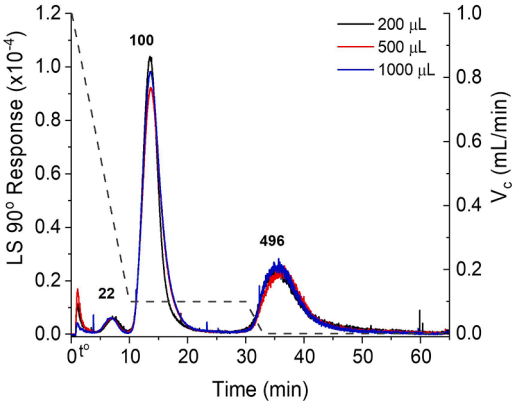

Fig. 1. AF4-MALS separation of a 22, 100, and 500 nm polystyrene latex mixture using 200, 500, and 1000 μL sample loops. The dashed line and right y-axis show the crossflow rate program.

successful separations (Figs. 1 and S1). Sample recovery, assessed by comparing the UV peak areas of the separated mixture with crossflow to the area of the peak observed without the crossflow (Fig. S1), was higher than the accepted sample recovery of >70 % across the three sample volumes [38] For the 22, 100, and 496 nm PSL standard mixture, the total sample recovery was estimated to be 81, 83, and 75 % for the 200, 500, and 1000 μL loops, respectively. Thus, the AF4 method used here is amenable to scale-up without significantly reduced sample recovery, and therefore 1000 μL loop was used for separation of the OMVs to maximize the amount of sample processed per run.

4.1.2. MALS particle counting: utilization of spherical models with PSL standards

To understand the limitations (model, particle size, etc.) associated with MALS particle counting, initial experiments were done with the PSL standards used in the AF4 method development as they are spherical shape and have a known RI value (1.58). Currently there is no count standard for < 1 μm particles or count standard for biological particles, which would provide a better model for assessing MALS particle counting for OMVs. As discussed in the MALS Particle Counting Theory section, the sphere and Lorenz-Mie models can be used to examine spherical particles. Since the 100 nm PSL particles would show some angular dependence on the light scattering signal and potentially be the upper limit of the sphere model, this size was used to examine changes in particle count between the two models. The 22 nm PSL sample could not be fit to either the sphere or the Lorenz-Mie models. This could be due to the lower size limitations of the MALS or the lower light scattering signal of this PSL size. The Lorenz-Mie model will only be utilized for the 496 nm PSL because of the strong forward scattering signal where the RGD approximation would no longer be satisfied. Based on the 1 % solids listed on the manufacturer's certification of analysis (CoA) and the known diameter of the particle size standard, one can calculate a nominal particle count using Eq. (3), where W_v% is the percent solids based on the CoA, ρ_p is the polymer microsphere density, and d is the diameter of the particle [39].

$$N_p = \frac{W_v\%\left(6.0x10^{10}\right)}{\pi\rho_p d^3} \tag{3}$$

Experimental particle counts compared to nominal values for the 100 nm PSL are shown in Fig. 2. The latter were determined using Eq. (3) based on the injected mass and recovery value of the 100 nm PSL. Both the sphere and Lorenz-Mie models exhibit linear trends and demonstrate the expected change in particle counts with an increase in injected sample concentration. Moreover, the sphere model more closely matched the expected slope of unity. The Lorenz-Mie model has consistently larger particle counts compared to the sphere model by 11–12 %.

One contribution to this observed difference between the two models could lie within the measurement of the particle size or volume. In both Eqs. S2 and 2 the (volume)^2 is inversely proportional to the number of particles per milliliter. Upon further investigation, online radius data showed minimal differences with uncertainty < 2 %. The other potential reason for this difference in slope is centered around the assumption $(n_a/n_o - 1 \ll 1)$. As the RI of the analyte (n_a) increases, the assumption becomes increasingly less valid. To demonstrate this, the RI value for PSL was varied from its known value of 1.58 to a range of 1.35–1.65. The results in Fig. 3 show an increasing percent difference in particle concentrations calculated using the two models as the analyte's RI increases. Between RI values of 1.55 and 1.60, the percent difference ranges between 10.1 and 13.3 %, correlating to differences in the counts between the sphere and Lorenz-Mie models seen in Fig. 2. The results of Fig. 3, supporting the differences observed in Fig. 2, highlight the limitation of the sphere model. This suggests that the Lorenz-Mie model may be more well-suited for samples with higher RI values as it is not impacted by the assumption of $n_a/n_o - 1 \ll 1$. While the sphere model can still be used for analytes of higher refractive index, the experimentally determined particle count may be underestimated due to this assumption.

In addition to the two different models, another component of data processing is the selection of the MALS detectors to be used for data analysis. It is suggested that the smaller angles should be selected to better satisfy the RGD approximation to help extrapolate the fitted data to the 0° angle [40,41]. Larger angles may also be selected as the more detectors used, the better representation of the sample. Currently there is no definitive recommendation for the number of angles that should be selected for accurate analyses with either the RGD approximation or Lorenz-Mie theory besides the aforementioned. Previous works have suggested that selecting 13 detectors should be sufficient to have a good representation of the analyte across all angles. This includes all models and analyte RI values. Higher noise at lower angles, however, may cause unattainable fits unless these lower angles are removed for both the sphere (RGD approximation) and Lorenz-Mie models [33,42].

Effects of selected detectors used for analysis of the 100 nm PSL can be seen in Fig. S2. Three detector ranges were investigated (2–18, 5–18, and 9–18) based on the correlation coefficient $R^{2'}$ values provided by the ASTRA software at peak maxima. These $R^{2'}$ values, associated with the MALS data processing step, are typically used to assess the goodness of the fit to the light scattering model. There were no significant changes in particle counts between selecting detectors 2–18 and 5–18 for either sphere or Lorenz-Mie models. However, the fits were drastically different with detectors 2–18 and 5–18 having $R^{2'}$ values of 0.05–0.07 and 0.6–0.7, respectively. While the smallest angles (detectors 2–4)

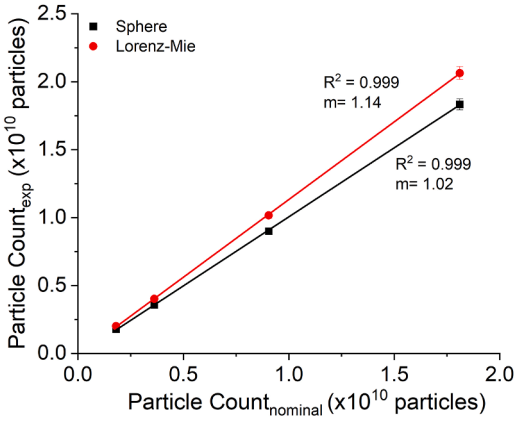

Fig. 2. Comparison of experimental and nominal particles counts using the sphere and Lorenz-Mie models for PSL standards. The nominal counts are based on a 200 μL injection volume and 1 % solid suspension of 100 nm PSL. Detectors 5–18 were used in this analysis.

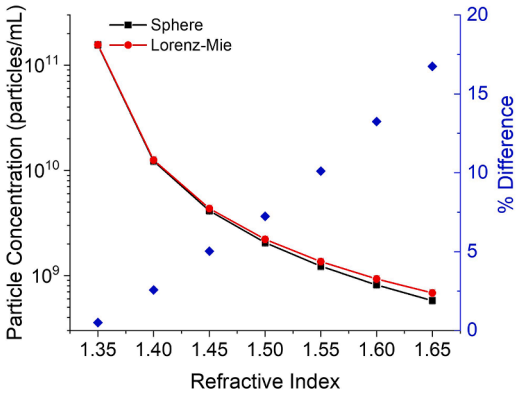

Fig. 3. Changes in particle concentration as a function of refractive index for 100 nm PSL particles using the sphere and Lorenz-Mie models.

should help satisfy the RGD approximation, they do not exhibit significantly different particle counts due to poor fitting of the data to each spherical model. Across both models, there is a difference in particle counts between the use of detectors 5–18 and 9–18 despite good linearity in the fit of the data points ($R^2 = 0.999$). This suggests that detector selection, in addition to model choice, can impact the calculated particle counts.

The 496 nm PSL particles were also examined considering the influences of MALS calculated counts, detector selection, and model choice. One major hindrance with a larger-sized population is that because light scatters more in the forward direction and to the diameter to the sixth power, saturation of the lower angled detectors (< detector 8, $\theta = 64°$) easily occurred at low concentrations. To mitigate this, the laser power of the MALS was decreased to 25 %, and lower concentrations were utilized. Additionally, because of the larger diameter (496 nm), only the Lorenz-Mie model could be assessed. Similar to Figs. 2 and S2, the 496 nm PSL shows a linear trend, but with much larger slopes (Fig. S3). Again, the linear trends suggest that MALS can provide a good correlation between increased concentration and increased particle counts, but absolute particle counts cannot be determined.

4.2. Separation and enumeration of *P. putida* OMVs using AF4-MALS

4.2.1. Size-based separation of *P. putida* OMVs

Given the methodological evaluations with a mixture of PSL standards, we next sought to apply the AF4-MALS method to bioparticles and evaluate the effect of key parameters, such as model and RI, on counts. To generate OMVs, *P. putida* was cultivated in lignin-free or lignin-rich media and bulk OMVs were harvested at 24 h from biological triplicates as previously described [34]. OMVs harvested from both types of media were anticipated to contain bimodal size populations. This expectation was based on prior results from dynamic light scattering measurements that showed two OMV subpopulations in both lignin-free ($\overline{d}$ = 17 and 120 nm) and lignin-rich ($\overline{d}$ = 28 and 307 nm) cultivations, respectively [34]. For OMV separation, an AF4 method with 1000 µL sample volume was applied to accomplish the following: (i) remove small particles ($d \approx 4$–6 nm, approximately the size of a single protein) in the focusing step, (ii) elute smaller OMVs rapidly thereafter, and (iii) elute the larger OMVs with intra-population separation (Fig. S4a).

AF4 separation, MALS signal, and radiii were similar for the lignin-rich and lignin-free OMVs across analytical replicates (Fig. 4a). The total OMV populations for lignin-free samples display a lower light scattering signal and a lower size range (d = 40–138 nm, both populations) compared to the lignin-rich OMVs (d = 32–404 nm, both populations), which is slightly larger than each anticipated size range [34]. Within the larger OMV population, the continuous increase in the radius demonstrates that intra-population separation is achieved (Fig. 4a).[29] To address the presence and characterize the smaller OMV population (d < 30 nm), AF4 experiments using an isocratic crossflow rate of 0.1 mL/min were performed on the lignin-rich samples (Fig. S4b). AF4 theory was then used to calculate the OMV size from the retention times in the MALS fractogram and yielded a range of 20–50 nm in diameter between 1.7 and 3.8 min. The average particle size of the collected fraction using batch DLS (Fig. S4b, shaded region) was 36 nm, confirming the presence of a smaller size population. Finally, AF4-MALS was conducted on the biological replicates for both the lignin-free and lignin-rich samples. AF4 retention times, MALS signal (LS 90° Response), and radius distributions were consistent across the triplicates in both media conditions (Fig. 4b and c). The higher signal-to-noise within the lignin-rich samples is due to the presence of larger particles, as light is scattered $\sim d^6$.

4.2.2. Estimation of OMV RI values for use in the coated-sphere model

The structure and composition of OMVs are more complex than PSL spheres and how to best represent these vesicles and the RI value(s) to use during count analysis by MALS need to be considered. The current understanding of *P. putida* OMVs suggests they should be modeled as a core-shell structure. Compositionally, the shell contains a mixture of lipopolysaccharides (LPS), phospholipids (PL), and transmembrane proteins while the core is filled primarily with water and protein, suggesting the core and shell may have different RI values. One major challenge with examining OMVs and other biological particles using light scattering is the lack of experimentally determined RI values or methods to easily obtain this information [43,44]. Few studies have utilized experimental data from techniques like NTA or flow cytometry scatter ratios (Flow- SR) of mammalian EVs to estimate RI values that span 1.35–1.40 [43]. One drawback is that these values may not effectively represent the OMVs used here due to differences in composition.

Taking a calculation approach, the RI values for OMVs were determined from the weight percent, partial specific volume of a sphere, and *dn/dc* values of the individual components. This approach has recently been used for MALS particle concentration determinations of lipid-based nanoparticles for RNA delivery [20]. A range of RI values for both the 'shell' and 'core' of the *P. putida* OMVs were calculated for a range of compositions. The RI value of the shell considered an LPS and PL bilayer in which transmembrane proteins are embedded. The ratio of LPS, PL, and protein was varied from no protein in the OMV shell (50:50:0 weight percent LPS:PL:protein) to more than half being protein (20:20:60 weight percent LPS:PL:protein). Similarly, core RI values for a range of water:protein content were determined (Table S2). The *dn/dc* values for LPS, PL, and protein used in these calculations of RI for different composition shell and core are summarized in Table S3 [20]. Shell and core RIs ranged from 1.49 to 1.52 and 1.33–1.58, respectively. While this range is broad, it encompasses a similar range of RI values determined for mammalian EVs [45–49].

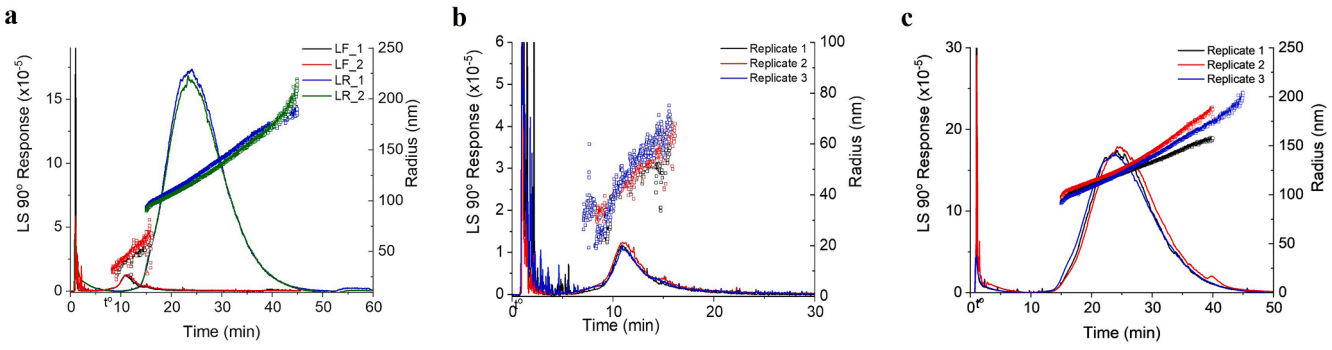

Fig. 4. (a) MALS responses and radius distributions across the AF4 separation of *P. putida* OMVs isolated from lignin-free (LF) and lignin rich (LR) cultivations. Reproducibility of three biological replicates of *P. putida* OMVs grown in (b) lignin-free and (c) lignin-rich media. Each MALS fractogram and radius distribution is an average of two AF4 injections.

4.2.3. Impacts of RI values and LS model on OMV particle counts

After verifying the AF4 separation was reproducible across biological replicates and estimated RI values were calculated, the impact of RI values and light scattering models on particle counts were examined. While both OMV size populations are present, only the larger vesicle populations eluting between 8 and 17 min. (lignin-free) and 15–40 min (lignin-rich) were considered for particle counting as they had the higher intensity of light scattering signal. The coated sphere model most closely approximated the OMV structure. The lipid bilayer thickness used for the coated sphere model was 4 nm. This was chosen based on existing literature values that ranged between 3 and 6 nm for various lipid compositions [50,51]. The sphere and Lorenz-Mie models were also assessed despite the sphere model potentially reaching its upper limit of ~100 nm. Moving forward, the RI value for the "core" of the coated sphere model will be termed "sphere RI."

Fig. 5 shows particle count as a function of RI for lignin-free and lignin-rich OMVs when different LS models are selected. For lignin-free OMVs, the coated sphere model gave rise to unrealistic particle counts ($> 10^{16}$ particles/mL) (Fig. 5a), likely owing to the poor signal-to-noise (S/N) observed for the MALS detector response (see Fig. 4a and b). This was confirmed when detailed examination of particle counts across the entirety of the peak within the ASTRA software showed anomalously large spikes that subsequently influenced the total particle count. This demonstrated the sensitivity of coated sphere model to the quality (S/N ratio) of the measured light scattering intensity. The sphere and Lorenz-Mie models showed similar particle counts; however, across the RI range of 1.35 to 1.65, a two order of magnitude change in particle counts is observed and is consistent for both OMV samples.

Unlike the lignin-free OMVs, the lignin-rich OMVs do not exhibit the anomalous higher particle counts for the coated sphere model (Fig. 5b). This is likely due to the lignin-rich OMVs exhibiting a larger S/N ratio LS intensity owing to their larger size. For a sphere RI value of 1.33, the coated sphere model behaves similarly to the sphere and Lorenz-Mie model but gives rise to a larger number of particles. With sphere RI values held constant at 1.43 or 1.53, the particle counts are stabilized across the shell RI values and at a constant shell thickness. These trends hint at the sphere RI in the coated sphere model having a greater influence than the shell RI or shell thickness on particle counts. The difference in magnitude of the particle counts between sphere RI values of 1.43 and 1.53 can be attributed to the ratio of analyte and solvent refractive index observed in the single particle scattering function i (θ) (Eq. (S2)). While this change in counts can be attributed to the sphere RI, this trend does not hold for the sphere RI of 1.33, as discussed in the next section on shell RI and shell thickness. With respect to using the sphere model for the lignin-rich samples, the overall trend in counts matched those using the Lorenz-Mie model which is unexpected. Despite the lignin-rich OMVs being larger in size, major differences in particle counts may not be observed due to the influence of detector selection as discussed earlier.

4.2.4. Impacts of shell thickness on OMV particle counts

As the sphere RI approaches or equals the RI value of the suspending fluid using the coated sphere model, particle counts appear to increase significantly (Fig. 5b, red trace). Because this trend deviates from the higher sphere RI values, the shell thickness and RI values could be influencing the magnitude of the particle counts. When examining different shell thickness values of 2, 4, and 6 nm across the different sphere RI values, a sphere value of 1.33 shows significant variation in the magnitude of particle counts with respect to shell RI and shell thickness (Fig. 6a) [52].

Based on the results from Fig. 5, it can be concluded that the counts are not affected by the shell RI or thickness (Fig. 6b and c). This reiterates that the dominating parameter in the coated sphere model is the sphere RI. In the case of unknown shell thickness and RI values, there is more leniency in the estimation of shell thickness compared to sphere RI values. Despite being a better representation of the OMVs, the sensitivity of the coated sphere model, which could be algorithm-dependent, does not allow accurate particle counting for the smaller OMVs due to the low S/N in the MALS intensity. Therefore, while the AF4 method is still suitable to separate particles in lignin-free and lignin-rich media, particle counts cannot be compared directly using the coated sphere model. One way to achieve a higher MALS signal so that the coated sphere model could be used in this application is through a concentration step after AF4 separation and prior to the analyte flowing into the MALS.

5. Conclusion

This work presents an AF4-MALS method for the simultaneous separation and enumeration of polydisperse bioparticles, including bacterial OMVs. This first-time detailed examination identified key parameters that impact MALS particle counts and demonstrated the *magnitude* of the impact of the light scattering model used in data analysis, RI values, and the signal-to-noise ratio of the MALS intensity. Bioparticle counts via MALS were found to be most suitable when shape and RI are known, and good signal-to-noise at all selected angles is achieved. In sum, AF4-MALS can be used as a separation, enumeration, and purification method for bioparticles such as OMVs but relies on careful consideration of key MALS parameters.

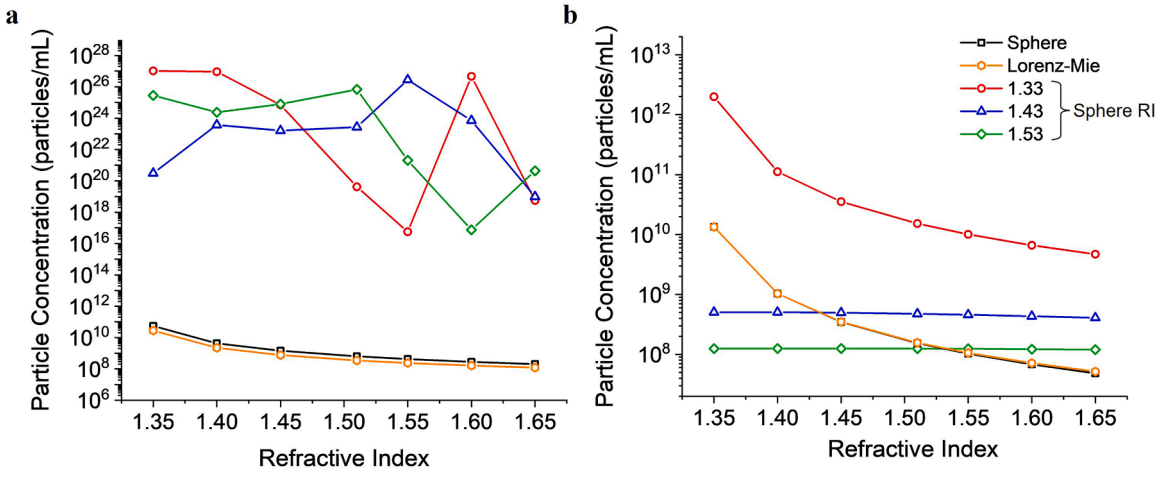

Fig. 5. Effect of RI values and light scattering model on particle concentration for (a) lignin-free and (b) lignin-rich samples. For the coated sphere model, the sphere RI value was kept constant at 1.33, 1.43, or 1.53 while the shell RI value (x-axis) was changed. The shell thickness was held constant at 6 nm. Data corresponds to fractograms shown in Fig. 4b and c.

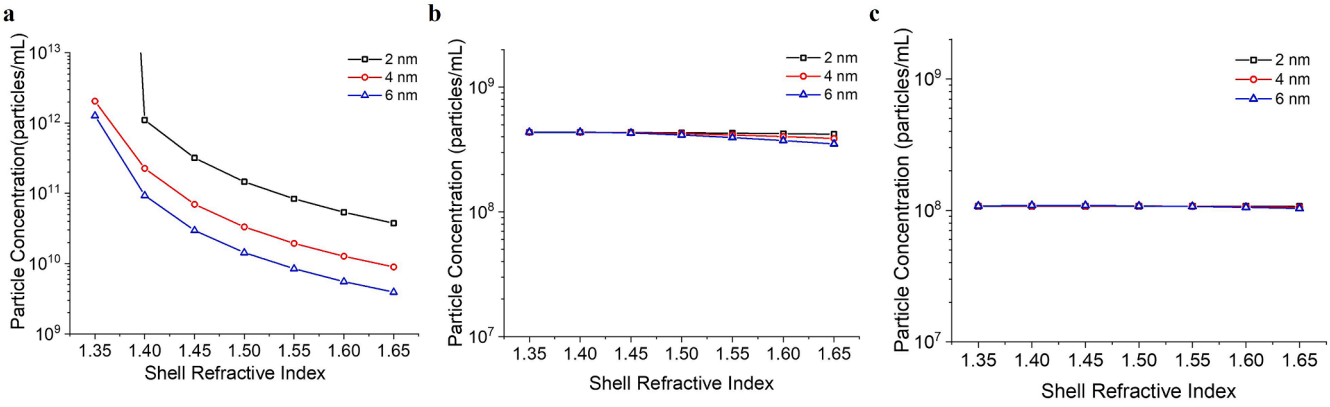

Fig. 6. Effect of shell thickness on particle counts using the coated sphere model for the peak in the MALS fractogram of Fig. 4c. The sphere RI was kept constant at (a) 1.33, (b) 1.43, or (c) 1.53 while changing shell RI value. For each sphere and shell RI value combination, the particle counts were calculated for shell thicknesses of 2, 4, and 6 nm.

The effect of light scattering theory was systematically evaluated for PSL standards and OMV bioparticles using sphere, Lorenz-Mie, and coated sphere models. Between the three spherical models studied, the coated sphere model is most sensitive to noise in the measured signal intensity; samples with $S/N > 800$ returned reasonable particle counts but were greatly influenced by the sphere RI. The sphere and Lorenz-Mie models are less sensitive to S/N, but a small RI range yields up to a 200 % variation in OMV particle counts. Deviations between results from the sphere and Lorenz-Mie models can be attributed to assumptions within the light scattering theory and warrant special consideration when working with materials that strongly scatter light. To address this, improved model fits utilizing lower detector angles would provide more accurate particle counts for both sphere and Lorenz-Mie models. This is especially important for the sphere model where the numerator of Eq. (2) heavily relies on the extrapolation of scattered light back to the 0° angle. Additional considerations such as the assessment of normalization constants and AF4 method optimization may also help with improved data fits for larger analytes. Moreover, the trends observed with PSL standards demonstrate appropriate and expected MALS responses, however only relative particle counts can be achieved. To determine absolute particle counts, a particle count standard with a closer refractive index to water (RI =1.33) would satisfy the assumptions made with the RGD approximation.

Considering the variables that impact counts reported by MALS for bioparticles, it is important to report the RI values used, the MALS detectors selected, the LS model used, and other processing parameters (e.g., despiking of LS signals). While biochemical analyses can inform the compositional ratio of biological particles and aid in calculating a more accurate RI, this remains a time-intensive process and is not a standard practice in the field. Thus, new methods for RI determination of bioparticles could aid in improving the accuracy of MALS particle counts and could impact other data analyses such as DLS.

Appendix-Supporting Information

MALS particle counting theory, AF4 method development using polystyrene latex beads, impacts of detector selection for polystyrene latex particles, table with literature *dn/dc* and RI values for OMV components, and detector number and corresponding angles for MALS instrumentation (PDF).

CRediT authorship contribution statement

Christine L. Plavchak: Writing – review & editing, Writing – original draft, Visualization, Methodology, Investigation, Formal analysis, Conceptualization. **Allison Z. Werner:** Writing – review & editing, Resources, Project administration, Conceptualization. **Elizabeth Betz:** Investigation, Formal analysis. **Davinia Salvachúa:** Writing – review & editing, Funding acquisition, Formal analysis. **Gregg T. Beckham:** Writing – review & editing, Funding acquisition, Formal analysis. **S. Kim Ratanathanawongs Williams:** Writing – review & editing, Visualization, Supervision, Project administration, Methodology, Conceptualization.

Declaration of competing interest

The authors declare that they have no known competing financial interests or personal relationships that could have appeared to influence the work reported in this paper.

Acknowledgements

This material is based upon work primarily supported by the National Science Foundation (NSF) under NSF Award CHE-1808805 (CLP, SKRW) along with the Colorado School of Mines Undergraduate Research Fellowship (EB). This work was authored by the Alliance for Sustainable Energy, LLC, the manager and operator of the National Renewable Energy Laboratory for the U.S. Department of Energy (DOE), under Contract No. DE-AC36-08GO28308 (CLP, AZW, DS, GTB). This material is based upon work supported by the Center for Bioenergy Innovation (CBI), U.S. Department of Energy, Office of Science, Biological and Environmental Research Program under Award Number ERKP886. The views expressed herein do not necessarily represent the views of the DOE or the U.S. Government. The U.S. Government retains and the publisher, by accepting the article for publication, acknowledges that the U.S. Government retains a non-exclusive, paid-up, irrevocable, worldwide license to publish or reproduce the published form of this work, or allow others to do so, for U.S. Government purposes. The authors would also like thank Wyatt Technology Corporation for the customer service support and suggestions.

Supplementary materials

Supplementary material associated with this article can be found, in the online version, at doi:10.1016/j.chroma.2024.465460.

Data availability

Data will be made available on request.

References

[1] J. Maia, S. Caja, M.C.S. Moraes, N. Couto, B. Costa-Silva, Exosome- based cell-cell communication in the tumor microenvironment, Front. Cell Dev. Biol. 6 (2018).

[2] A. Ziegenbalg, R. Prados-Rosales, E.R. Jenny-Avital, R.S. Kim, A. Casadevall, J. M. Achkar, Immunogenicity of mycobacterial vesicles in humans: identification of a new tuberculosis antibody biomarker, Tuberculosis 93 (2013) 448–455, https://doi.org/10.1016/j.tube.2013.03.001.

[3] M.C. Ciferri, R. Quarto, R. Tasso, S. Bernardi, Extracellular vesicles as biomarkers and therapeutic tools: from pre-clinical to clinical applications, Biology 10 (2021) 359, https://doi.org/10.3390/biology (Basel).

[4] Z.E. Suntres, M.G. Smith, F. Momen-Heravi, J. Hu, X. Zhang, Y. Wu, H. Zhu, J. Wang, J. Zhou, W.P. Kuo, Therapeutic uses of exosomes, J. Circ. Biomark. 1 (2013), https://doi.org/10.5772/56522.

[5] R. Vogel, J. Savage, J. Muzard, G. Della Camera, G. Vella, A. Law, M. Marchioni, D. Mehn, O. Geiss, B. Peacock, D. Aubert, L. Calzolai, F. Caputo, A. Prina-Mello, Measuring particle concentration of multimodal synthetic reference materials and extracellular vesicles with orthogonal techniques: who is up to the challenge? J. Extracell. Vesicles 10 (2021) https://doi.org/10.1002/jev2.12052.

[6] F.A.W. Coumans, E. Van Der Pol, A.N. Böing, N. Hajji, G. Sturk, T.G. Van Leeuwen, R. Nieuwland, A.N. Bö Ing, Reproducible extracellular vesicle size and concentration determination with tunable resistive pulse sensing, J. Extracell. Vesicles 3 (2014), https://doi.org/10.3402/jev.v3.25922.

[7] P. Terejánszky, I. Makra, P. Fürjes, R. Róbert, R.E. Gyurcsányi, Calibration-less sizing and quantitation of polymeric nanoparticles and viruses with quartz nanopipets, Anal. Chem. 86 (2014) 4688–4697, https://doi.org/10.1021/ac500184z.

[8] S. Vaidyanathan, H. Wijerathne, S.S.T. Gamage, F. Shiri, Z. Zhao, J. Choi, S. Park, M.A. Witek, C. McKinney, M. Verber, A.R. Hall, K. Childers, T. McNickle, S. Mog, E. Yeh, A.K. Godwin, S.A. Soper, High sensitivity extended nano-coulter counter for detection of viral particles and extracellular vesicles, Anal. Chem. 95 (2023) 9892–9900, https://doi.org/10.1021/acs.analchem.3c00855.

[9] I. Makra, P. Terejánszky, R.E. Gyurcsányi, A method based on light scattering to estimate the concentration of virus particles without the need for virus particle standards, MethodsX (2015) 91–99, https://doi.org/10.1016/j.mex.2015.02.003.

[10] V. Filipe, A. Hawe, W. Jiskoot, Critical evaluation of nanoparticle tracking analysis (NTA) by NanoSight for the measurement of nanoparticles and protein aggregates, Pharm. Res. 27 (2010) 796–810, https://doi.org/10.1007/s11095-010-0073-2.

[11] Z. Wei, M. McEvoy, V. Razinkov, A. Polozova, E. Li, J. Casas-Finet, G.I. Tous, P. Balu, A.A. Pan, H. Mehta, M.A. Schenerman, Biophysical characterization of influenza virus subpopulations using field flow fractionation and multiangle light scattering: correlation of particle counts, size distribution and infectivity, J. Virol. Methods 144 (2007) 122–132, https://doi.org/10.1016/j.jviromet.2007.04.008.

[12] C. Gardiner, Y.J. Ferreira, R.A. Dragovic, C.W.G. Redman, I.L. Sargent, Extracellular vesicle sizing and enumeration by nanoparticle tracking analysis, J. Extracell. Vesicles 2 (2013), https://doi.org/10.3402/jev.v2i0.19671.

[13] D. Bachurski, M. Schuldner, P.-H. Nguyen, A. Malz, K.S. Reiners, P.C. Grenzi, F. Babatz, A.C. Schauss, H.P. Hansen, M. Hallek, E. Pogge, V. Strandmann, Extracellular vesicle measurements with nanoparticle tracking analysis–an accuracy and repeatability comparison between NanoSight NS300 and ZetaView, J. Extracell. Vesicles 8 (2019), https://doi.org/10.1080/20013078.2019.1596016.

[14] M. Andersson, B. Wittgren, K.G. Wahlund, Accuracy in multiangle light scattering measurements for molar mass and radius estimations. Model calculations and experiments, Anal. Chem. 75 (2003) 4279–4291, https://doi.org/10.1021/ac030128. +.

[15] S. Sitar, A. Kejž, D. Pahovnik, K. Kogej, M. Tušek-Znidarič, M. Lenassi, E. Zagar, Size characterization and quantification of exosomes by asymmetrical-flow field-flow fractionation, Anal. Chem. 87 (2015) 9225–9233, https://doi.org/10.1021/acs.analchem.5b01636.

[16] P. Steppert, D. Burgstaller, M. Klausberger, A. Tover, E. Berger, A. Jungbauer, Quantification and characterization of virus-like particles by size-exclusion chromatography and nanoparticle tracking analysis, J. Chromatogr. A 1487 (2017) 89–99, https://doi.org/10.1016/j.chroma.2016.12.085.

[17] G.B. Adkins, E. Sun, R. Coreas, W. Zhong, Asymmetrical flow field flow fractionation coupled to nanoparticle tracking analysis for rapid online characterization of nanomaterials, Anal. Chem. 92 (2020) 7071–7078, https://doi.org/10.1021/acs.analchem.0c00406.

[18] J. Parot, D. Mehn, H. Jankevics, N. Markova, M. Carboni, C. Olaisen, A.D. Hoel, M. S. Sigfúsdóttir, F. Meier, R. Drexel, G. Vella, B. McDonagh, T. Hansen, H. Bui, G. Klinkenberg, T. Visnes, S. Gioria, P. Urban-Lopez, A. Prina-Mello, S.E. Borgos, F. Caputo, L. Calzolai, Quality assessment of LNP-RNA therapeutics with orthogonal analytical techniques, J. Control. Release 367 (2024) 385–401, https://doi.org/10.1016/j.jconrel.2024.01.037.

[19] W. Gao, J. Cohen, F. Acholla, W. Su, Development of asymmetrical flow field fractionation with on-line advanced detections for particle size distribution analysis of silica colloidal particles, ACS Symp. Ser. 1281 (2018) 111–143, https://doi.org/10.1021/bk-2018-1281.ch007.

[20] R. Mildner, S. Hak, J. Parot, A. Hyldbakk, S.E. Borgos, D. Some, C. Johann, F. Caputo, Improved multidetector asymmetrical-flow field-flow fractionation method for particle sizing and concentration measurements of lipid-based nanocarriers for RNA delivery, Eur. J. Pharm. Biopharm. 163 (2021) 252–265, https://doi.org/10.1016/j.ejpb.2021.03.004.

[21] A. Parupudi, F. Gruia, S.A. Korman, S. Dragulin-Otto, K. Sra, R.L. Remmele, J. S. Bee, Biophysical characterization of influenza A virions, J. Virol. Methods 247 (2017) 91–98, https://doi.org/10.1016/j.jviromet.2017.06.002.

[22] H. Zhang, D. Lyden, Asymmetric-flow field-flow fractionation technology for exomere and small extracellular vesicle separation and characterization, Nat. Protoc. 14 (2019) 1027–1053, https://doi.org/10.1038/s41596-019-0126-x.

[23] H. Zhang, D. Freitas, H.S. Kim, K. Fabijanic, Z. Li, H. Chen, M.T. Mark, H. Molina, A.B. Martin, L. Bojmar, J. Fang, S. Rampersaud, A. Hoshino, I. Matei, C.M. Kenific, M. Nakajima, A.P. Mutvei, P. Sansone, W. Buehring, H. Wang, J.P. Jimenez, L. Cohen-Gould, N. Paknejad, M. Brendel, K. Manova-Todorova, A. Magalhães, J. A. Ferreira, H. Osório, A.M. Silva, A. Massey, J.R. Cubillos-Ruiz, G. Galletti, P. Giannakakou, A.M. Cuervo, J. Blenis, R. Schwartz, M.S. Brady, H. Peinado, J. Bromberg, H. Matsui, C.A. Reis, D. Lyden, Identification of distinct nanoparticles and subsets of extracellular vesicles by asymmetric flow field-flow fractionation, Nat. Cell Biol. 20 (2018) 332–343, https://doi.org/10.1038/s41556-018-0040-4.

[24] R.M.F. van der Put, A. Spies, B. Metz, D. Some, R. Scherrers, R. Pieters, M. Danial, Validation of an FFF-MALS method to characterize the production and functionalization of outer-membrane vesicles for conjugate vaccines, Anal. Chem. 94 (2022) 12033–12041, https://doi.org/10.1021/acs.analchem.2c01590.

[25] F. Dell'annunziata, V. Folliero, R. Giugliano, A. De Filippis, C. Santarcangelo, V. Izzo, M. Daglia, M. Galdiero, C.R. Arciola, G. Franci, A. Belén Flórez, Molecular sciences gene transfer potential of outer membrane vesicles of gram-negative bacteria, Int. J. Mol. Sci. 5985 (2021), https://doi.org/10.3390/ijms.

[26] S.L. Reimer, D.R. Beniac, S.L. Hiebert, T.F. Booth, P.M. Chong, G.R. Westmacott, G. G. Zhanel, D.C. Bay, Comparative analysis of outer membrane vesicle isolation methods with an Escherichia coli tolA mutant reveals a hypervesiculating phenotype with outer-inner membrane vesicle content, Front. Microbiol. 12 (2021), https://doi.org/10.3389/fmicb.2021.628801.

[27] C. Schwechheimer, M.J. Kuehn, Outer-membrane vesicles from Gram-negative bacteria: biogenesis and functions, Nat. Rev. Microbiol. 13 (2015) 605–619, https://doi.org/10.1038/nrmicro3525.

[28] T. Nagakubo, N. Nomura, M. Toyofuku, Cracking open bacterial membrane vesicles, Front. Microbiol. 10 (2020), https://doi.org/10.3389/fmicb.2019.03026.

[29] Wyatt Technology Corporation, DAWN® user's guide, 2020.

[30] P.J. Wyatt, M.J. Weida, Method and apparatus for determining absolute number densities of particles in solution, US 6,774,994 B1, 2004.

[31] D.J. Lockwood, Rayleigh and mie scattering. Encyclopedia of Color Science and Technology, Springer, 2016, pp. 1097–1107, https://doi.org/10.1007/978-1-4419-8071-7.

[32] D.M. Lawler, Turbidimetry and nephelometry. Encyclopedia of Analytical Science, Elsevier, 2005, pp. 343–351.

[33] P.J. Wyatt, Measurement of special nanoparticle structures by light scattering, Anal. Chem. 86 (2014) 7171–7183, https://doi.org/10.1021/ac500185w.

[34] D. Salvachúa, A.Z. Werner, I. Pardo, M. Michalska, B.A. Black, B.S. Donohoe, S. J. Haugen, R. Katahira, S. Notonier, K.J. Ramirez, A. Amore, S.O. Purvine, E. M. Zink, P.E. Abraham, R.J. Giannone, S. Poudel, P.D. Laible, R.L. Hettich, G. T. Beckham, Outer membrane vesicles catabolize lignin-derived aromatic compounds in Pseudomonas putida KT2440, PNAS 117 (2020) 9302–9310, https://doi.org/10.1073/pnas.1921073117.

[35] J.G. Linger, D.R. Vardon, M.T. Guarnieri, E.M. Karp, G.B. Hunsinger, M.A. Franden, C.W. Johnson, G. Chupka, T.J. Strathmann, P.T. Pienkos, G.T. Beckham, Lignin valorization through integrated biological funneling and chemical catalysis, PNAS 111 (2014) 12013–12018, https://doi.org/10.1073/pnas.1410657111.

[36] M. Leeman, J. Choi, S. Hansson, M.U. Storm, L. Nilsson, Proteins and antibodies in serum, plasma, and whole blood-size characterization using asymmetrical flow field-flow fractionation (AF4), Anal. Bioanal. Chem. 410 (2018) 4867–4873, https://doi.org/10.1007/s00216-018-1127-2.

[37] Z. Gao, Z. Hutchins, Z. Li, W. Zhong, Offline coupling of asymmetrical flow field-flow fractionation and capillary electrophoresis for separation of extracellular vesicles, Anal. Chem. 94 (2022) 14083–14091, https://doi.org/10.1021/acs.analchem.2c03550.

[38] F. Caputo, R. Vogel, J. Savage, G. Vella, A. Law, G. Della Camera, G. Hannon, B. Peacock, D. Mehn, J. Ponti, O. Geiss, D. Aubert, A. Prina-Mello, L. Calzolai, Measuring particle size distribution and mass concentration of nanoplastics and microplastics: addressing some analytical challenges in the sub-micron size range, J. Colloid Interface Sci. 588 (2021) 401–417, https://doi.org/10.1016/j.jcis.2020.12.039.

[39] Thermofisher Scientific, Useful latex bead formulae, (2024). https://www.thermofisher.com/us/en/home/life-science/cell-analysis/qdots-microspheres-nanospheres/idc-surfactant-free-latex-beads/latex-bead-technical-overview/useful-latex-bead-formulae.html (accessed June 24, 2024).

[40] Wyatt Technology Corporation, ASTRA ® 7.3 user's guide, 2019.

[41] M. Kerker, The Scattering of Light and Other Electromagnetic Radiation, Academic Press, New York, 1969.

[42] P. Kratochvil, Classical Light Scattering from Polymer Solutions, Elsevier, New York, NY, 1987.

[43] J.A. Welsh, E. Van Der Pol, B.A. Bettin, D.R.F. Carter, A. Hendrix, M. Lenassi, Towards defining reference materials for measuring extracellular vesicle refractive index, epitope abundance, size and concentration, J. Extracell. Vesicles 9 (2020) 1816641–1816657, https://doi.org/10.1080/20013078.2020.1816641.

[44] M.I. Ramirez, M.G. Amorim, C. Gadelha, I. Milic, J.A. Welsh, V.M. Freitas, M. Nawaz, N. Akbar, Y. Couch, L. Makin, F. Cooke, A.L. Vettore, P.X. Batista, R. Freezor, J.A. Pezuk, L. Rosa-Fernandes, A.C.O. Carreira, A. Devitt, L. Jacobs, I. T. Silva, G. Coakley, D.N. Nunes, D. Carter, G. Palmisano, E. Dias-Neto, Technical challenges of working with extracellular vesicles, Nanoscale 10 (2018) 881–906, https://doi.org/10.1039/c7nr08360b.

[45] E. van der Pol, F.A.W. Coumans, A.E. Grootemaat, C. Gardiner, I.L. Sargent, P. Harrison, A. Sturk, T.G. van Leeuwen, R. Nieuwland, Particle size distribution of exosomes and microvesicles determined by transmission electron microscopy, flow cytometry, nanoparticle tracking analysis, and resistive pulse sensing, J. Thromb. Haemost. 12 (2014) 1182–1192, https://doi.org/10.1111/jth.12602.

[46] C. Gardiner, M. Shaw, P. Hole, J. Smith, D. Tannetta, C.W. Redman, I.L. Sargent, Measurement of refractive index by nanoparticle tracking analysis reveals

heterogeneity in extracellular vesicles, J. Extracell. Vesicles 3 (2014) 1–6, https://doi.org/10.3402/jev.v3.25361.
[47] E. Van Der Pol, L. De Rond, F.A.W. Coumans, E.L. Gool, A.N. Böing, A. Sturk, R. Nieuwland, Absolute sizing and label-free identification of extracellular vesicles by flow cytometry LPs EVs, Nanomedicine 14 (2018) 801–810, https://doi.org/10.1016/j.nano.2017.12.012.
[48] E. Geeurickx, J. Tulkens, B. Dhondt, J. Van Deun, L. Lippens, G. Vergauwen, E. Heyrman, D. De Sutter, K. Gevaert, F. Impens, I. Miinalainen, P. Van Bockstal, T. De Beer, M.H.M. Wauben, R. Nieuwland, G. Braems, N. Callewaert, P. Mestdagh, J. Vandesompele, The generation and use of recombinant extracellular vesicles as biological reference material, Nat. Commun. 10 (2019) 3288–3298, https://doi.org/10.1038/s41467-019-11182-0.
[49] L. De Rond, S.F.W.M. Libregts, L.G. Rikkert, C.M. Hau, E. Van Der Pol, R. Nieuwland, T.G. Van Leeuwen, Refractive index to evaluate staining specificity of extracellular vesicles by flow cytometry, J. Extracell. Vesicles 8 (2019), https://doi.org/10.1080/20013078.2019.1643671.
[50] H. Trauble, D.H. Haynes, The volume change in lipid bilayer lamellae at the crystalline-liquid crystalline phase transition, Chem. Phys. Lipids 7 (1971) 324–335.
[51] D. Regan, J. Williams, P. Borri, W. Langbein, lipid bilayer thickness measured by quantitative DIC reveals phase transitions and effects of substrate hydrophilicity, Langmuir 35 (2019) 13805–13814, https://doi.org/10.1021/acs.langmuir.9b02538.
[52] N.C. Santos, A.C. Silva, M.A.R.B. Castanho, J. Martins-Silva, C. Saldanha, Evaluation of lipopolysaccharide aggregation by light scattering spectroscopy, ChemBioChem 4 (2003) 96–100.